Supplement of Atmos. Chem. Phys., 21, 1085–1104, 2021
https://doi.org/10.5194/acp-21-1085-2021-supplement

Atmospheric Chemistry and Physics
Open Access
EGU

Supplement of

Characteristics of sub-10 nm particle emissions from in-use commercial aircraft observed at Narita International Airport

Nobuyuki Takegawa et al.

Correspondence to: Nobuyuki Takegawa (takegawa@tmu.ac.jp)

Supplement

S1 Penetration efficiencies of particles through the sampling tubes

The penetration efficiencies of particles through the sampling tubes were estimated by using the theoretical formulae proposed by Gormley and Kennedy (1949). The calculations assumed a laminar flow at a pressure of 101 kPa and a temperature of 293 K. The inlet system was divided into the subsections listed in Table S1, and the overall penetration efficiency was derived as a product of the penetration efficiencies through the subsections. The subsection "UCPC internal" in Table S1 represents the effective tube length that can reproduce the penetration efficiency through a UCPC 3776 (Wimmer et al., 2013). The detection efficiencies of the UCPC and CPC, which are denoted as $\varepsilon_{\mathrm{UCPC}}$ and $\varepsilon_{\mathrm{CPC}}$, were set as follows based on our previous studies (Takegawa and Sakurai, 2011; Takegawa et al., 2017):

$$\varepsilon_{\mathrm{UCPC}} = \left(1 + \exp\left(\frac{2.50 - D}{0.111}\right)\right)^{-1}$$

$$\varepsilon_{\mathrm{CPC}} = 1 - \exp\left(\frac{6.99 - D}{4.78}\right)$$

where D is the particle diameter. Note that the detection efficiency for the UCPC was empirically determined so as to satisfy $\varepsilon_{\mathrm{UCPC}}$ = ~0, 0.5, ~1 at diameters of <2, 2.5, >3 nm, respectively. This assumption does not significantly affect the major conclusions because the contributions of particles at 2–3 nm were minor in the theoretical calculations (Figs. 9 and 10). As shown in Fig. 3, the detection efficiencies of the UCPC and CPC incorporating the penetration efficiencies of the subsections agreed well with the experimental data.

Fig. S1 shows the penetration efficiency for the UCPC/CPC sampling line under the unheated mode (UCPC/CPC main × UCPC/CPC total sample × Unheated), that for the SMPS sampling line under the unheated mode (UCPC/CPC main × UCPC/CPC total sample × Unheated × SMSP sample), and that for the EEPS sampling line (EEPS main × EEPS sample). The penetration efficiency through the evaporation tube and the detection efficiencies of the UCPC and CPC were evaluated separately from the above estimates (see Section 3.1).

Table S1: Parameters for calculating the penetration efficiencies of particles for the UCPC, CPC, SMPS, and EEPS.

Subsection	Flow rate (L min^{-1})	Length (cm)	Penetration efficiency at 10 nm
UCPC/CPC main (rooftop – branch)	20	280	0.97
UCPC/CPC total sample (branch – mixing junction)	0.7	30	0.94
Unheated (mixing junction – splitter)	2.7	67	0.96
Heated (mixing junction – heater – splitter)	2.7	152	0.92
UCPC sample (splitter – UCPC)	1.4	50	0.94
CPC sample (splitter – CPC)	1.0	90	0.90
SMPS sample (splitter – SMPS)	0.3	100	0.77
UCPC internal	0.3	19	0.92
EEPS main (rooftop – manifold branch)	20	276	0.97
EEPS sample (manifold branch – EEPS)	10	100	0.97

Note: See Fig. 2 for the schematics of the subsections. The flow rate and length of each section are approximate values.

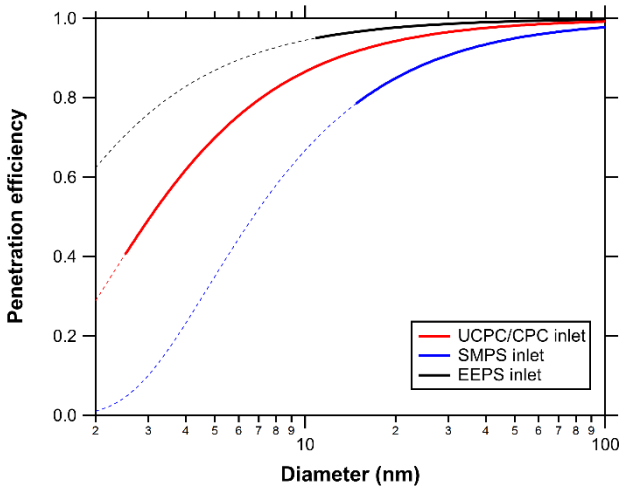

Figure S1: Penetration efficiencies of particles through the sampling lines for the UCPC/CPC (red), SMPS (blue), and EEPS (black) at room temperature (293 K) estimated by using the theoretical formulae proposed by Gormley and Kennedy (1949). The detectable size ranges for the UCPC, SMPS, and EEPS are indicated by solid lines. The calculated curve for the UCPC/CPC includes the penetration efficiency through the UCPC/CPC main, UCPC/CPC total sample, and Unheated subsections. The calculated curve for the SMPS includes the penetration efficiencies through the UCPC/CPC main, UCPC/CPC total sample, Unheated, and SMSP sample subsections. The calculated curve for the EEPS includes the penetration efficiencies through the EEPS main and EEPS sample subsections.

S2 Diffusion correction for the SMPS

The Aerosol Instrument Manager (AIM) software provides correction tools for these factors. We used AIM version 9.0 for the present analysis, with the diffusion loss correction enabled. Fig. S2 shows a comparison of the SMPS size distribution at 14:10 on February 15, 2018 with and without the AIM diffusion correction. The degree of correction was significant at smaller diameters. Nevertheless, the overall size dependency (i.e., increasing particle number concentrations with decreasing particle diameters below 20 nm) is consistent between the SMPS and EEPS data, regardless of the AIM diffusion correction.

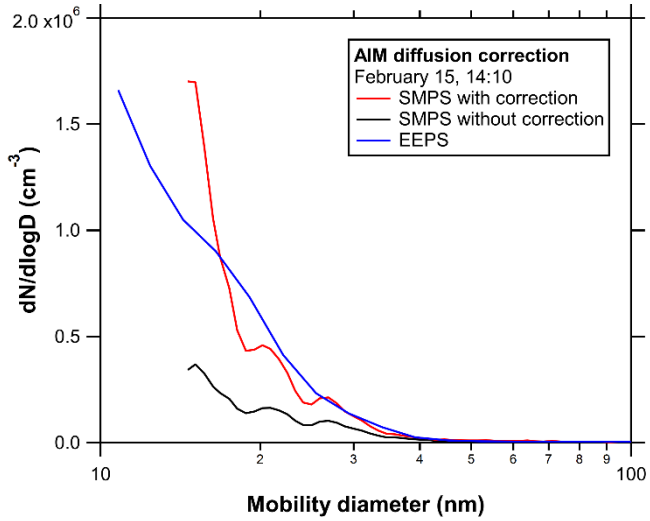

Figure S2: Particle number size distributions measured simultaneously by the EEPS and unheated SMPS (with and without the AIM diffusion correction) for the selected time period indicated in Fig. 6.

S3 Plume analysis

In the observed air parcels, aircraft emissions from take-off, landing, and idling phases may have been mixed in the atmosphere, and the characterization of particle emissions should be performed carefully. The distance from the observation point to the taxiway was ~380 m and that to the gate was >800 m. We expected that aircraft emissions during idling would contribute to relatively broad, diffuse increases in aerosols and CO_2 and that those during take-off and landing would appear as spiked increases in aerosols and CO_2 at the observation point.

To extract discrete plumes originating from individual aircraft during take-off or landing, we defined background levels for $N_{2.5}$, N_{10}, and CO_2, and calculated enhancements above the background levels ($\Delta N_{2.5}$, ΔN_{10}, and ΔCO_2). The background estimate is more critical for CO_2. For air parcels originating from the runway (wind directions from north to east-southeast, wind speeds of >1 m s^{-1}), the sets of air parcels that were selected by the following procedures were defined as "plumes":

(a) The background air was defined as satisfying the following conditions: $| dCO_2/dt | < 0.1$ ppmv s^{-1}, $| d^2CO_2/dt^2 | < 0.1$ ppmv s^{-2}, $| dN_{10}/dt | < 500$ cm^{-3} s^{-1}, and $N_x < N_{th}$, (x = 2.5 or 10) where d/dt represents the time differential. The second and fourth conditions were set to exclude plume peaks. The threshold value, N_{th}, depended on the meteorological conditions and was set to an appropriate values for each day.

(b) The above background values were interpolated to determine the baselines for $N_{2.5}$, N_{10}, and CO_2. The baseline was subtracted to obtain $\Delta N_{2.5}$, ΔN_{10}, and ΔCO_2.

(c) If the peak ΔCO_2 exceeded 15 ppmv, the ΔCO_2 values decreased to below 10% of the peak value within 60 s before or after the peak, and the duration of the enhancement was longer than 30 s, the set of air parcels was selected as a "plume".

The above threshold values were determined by considering the observed shapes of the CO_2 and aerosol spikes. Step (a) was used to identify "stable" baseline data points, and the conditions were set as redundant. The criterion of 10% in step (c) eliminated overlaps of multiple plumes. This automated procedure may have discarded some possible plume events, depending on the meteorological condition. Nevertheless, we chose these criteria to avoid subjective biases.

Next, the $\Delta N_{2.5}/\Delta CO_2$, $\Delta N_{10}/\Delta CO_2$, and $\Delta N_{10}/\Delta N_{2.5}$ ratios for the identified plumes were calculated. Only data with N_{10} smaller than 5×10^5 cm^{-3} (~1×10^5 cm^{-3} downstream of the dilution section) were used for the analysis because the uncertainty due to particle coincidence increases at higher concentrations. Data obtained on February 15, 16, 20, 21, and 22 were used for the plume analysis. The $\Delta N_{2.5}/\Delta CO_2$, $\Delta N_{10}/\Delta CO_2$, and $\Delta N_{10}/\Delta N_{2.5}$ ratios were calculated by using an area-integration method, similar to that used by Moore et al. (2017a). We also calculated these ratios as linear regression slopes after the data points were averaged over 3 s. The data average was used to account for differences in the response times of the instruments. Although these two methods generally showed reasonable agreement, there were significant discrepancies in some cases, especially at low r^2 values by the regression method. The reason for the discrepancy at low r^2 values was that the temporal variations in $N_{2.5}$ and N_{10} did not track well with that of CO_2. A possible explanation for this feature is that particle

emissions might vary significantly during take-off (e.g., a burst of soot particles in the initial stages), as pointed out by Moore et al. (2017a).

The arrival time of a plume was estimated by considering the wind directions and speeds, assuming that the time for the plume to traverse from the centerline of the runway to the observation point was controlled by the wind vector component perpendicular to the runway. The duration of a plume was estimated from the time difference between the two 10%-crossing points defined in step (c) (when the ΔCO_2 values decreased to below 10% of the peak value within 60 s before or after the peak). The estimated arrival time of plumes was ~30–120 s, which corresponds to the transport distance of ~180–370 m.

The flight-schedule table provided by NRT, which specified the take-off or landing times of specific aircraft with a time resolution of 1 min, was used to investigate the statistics of aircraft take-offs and landings. During the time periods of the plume analyses, 80–90% of the aircraft that passed along the runway were in the take-off phase. The flight schedule table, estimated arrival times, and our video-camera records (only during the daytime) were used to attribute the observed plumes to take-off or landing phases. Fig. S3 shows an example of the correspondence between the plume events and the flight information. Aerosol particle number concentrations for diameters larger than 7 nm (N_7) as measured by the undiluted and unheated CPC 3022 are shown for comparison. In Fig. S3a, we can see a reasonably good agreement between N_7 and N_{10}, as expected. In Fig. S3b, the depletion of aerosol particle number concentrations upon heating is evident.

Although the observed plumes could, in most cases, be attributed to the take-off or landing of specific aircraft, there were some cases in which the one-to-one correspondence was somewhat ambiguous (shown as “unidentified” in Fig S3a). We attributed 132 plumes to take-offs for the unheated mode and 63 plumes to the 350°C heated mode. Potential uncertainties in the attribution (i.e., a landing plume incorrectly assigned to a take-off plume) were 10–20% at most, considering that 80–90% of the aircraft that passed along the runway were in the take-off phase. Table S2 shows the statistical summary of the particle number EIs classified by major aircraft models identified in this study. We did not observe a significant difference in the particle number EIs among these models, although there might be uncertainties in the attribution, as mentioned above.

Fig. S4 shows histograms of the estimated arrival time and duration of the plumes. Although our sampling conditions differed from those given by Moore et al. (2017a), the estimated arrival and duration times were comparable to their values. We did not find a systematic dependence of the $\Delta N_{10}/\Delta CO_2$ and $\Delta N_{2.5}/\Delta CO_2$ ratios on the arrival time of the plumes, as indicated in Fig. S5.

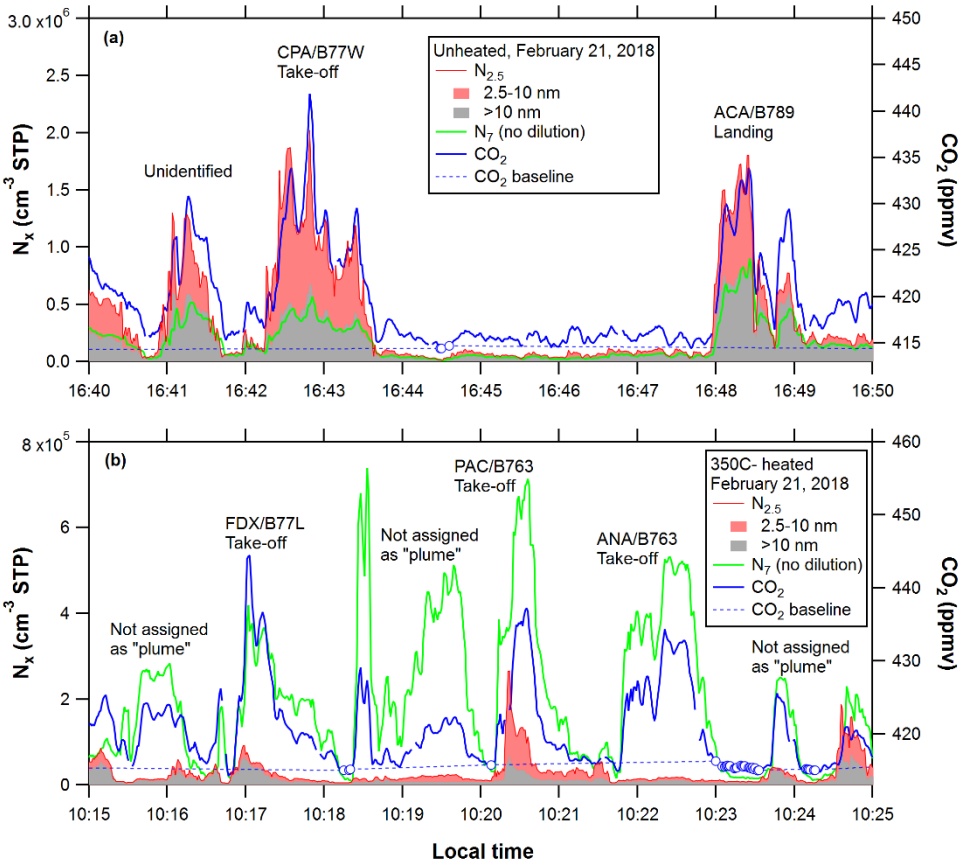

120 **Figure S3:** Examples of discrete plumes. Data for (a) unheated and (b) 350°C heated mode observed on February 21, 2018. Slight differences in the peak timing for very sharp spikes may be affected by the instrument response times. The blue open circles represent the estimated "background" concentrations for CO_2, and the blue dashed lines represent the interpolated background levels.

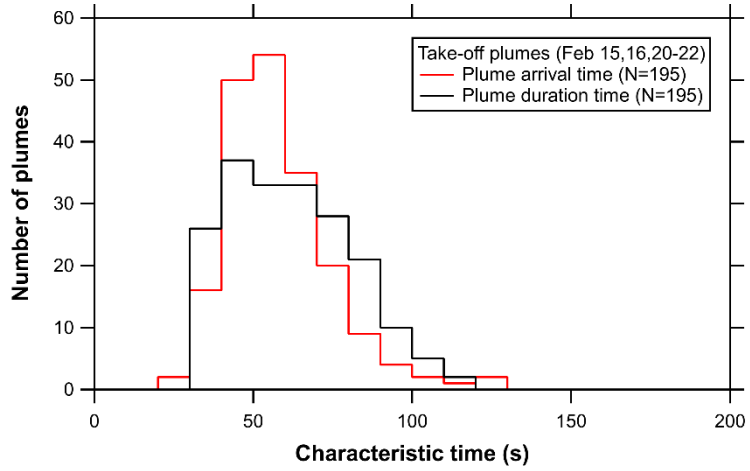

Figure S4: Histograms of the estimated arrival time and duration of plumes. The lower and upper limits of the duration time (30 s and 120 s, respectively) were determined by the definition of plumes.

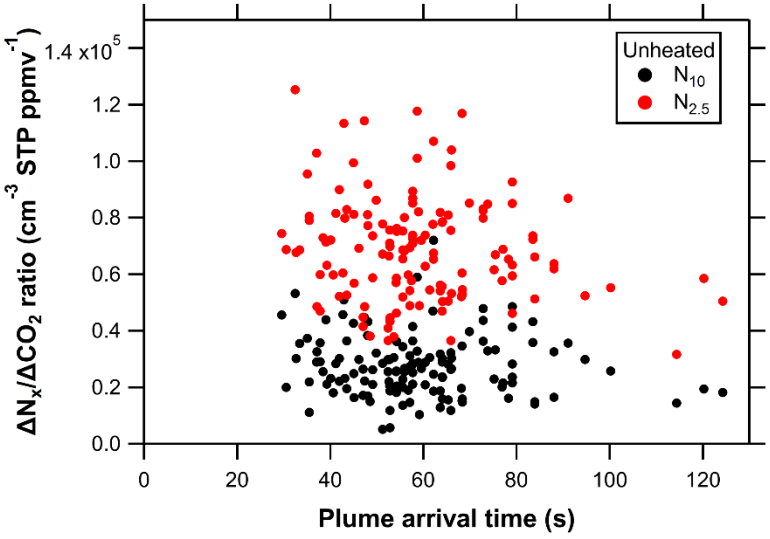

Figure S5: Dependence of $\Delta N_{2.5}/\Delta CO_2$ and $\Delta N_{10}/\Delta CO_2$ ratios on the arrival time of plumes.

Table S2: Medians of particle number EIs for take-off plumes classified by major aircraft models identified in this study (number of samples ≥ 5). The unit of particle number EIs is 10^{15} kg-fuel^{-1}.

Aircraft model	Total				Non-volatile			
	Number of samples	EI($N_{2.5}$)	EI(N_{10})	Sub-10 nm fraction	Number of samples	EI($N_{2.5}$)	EI(N_{10})	Sub-10 nm fraction
A320	12	80	44	0.44	N/A	N/A	N/A	N/A
A321	N/A	N/A	N/A	N/A	6	3.6	2.3	0.44
A333	21	94	35	0.65	9	2.4	1.2	0.49
B738	9	117	45	0.56	N/A	N/A	N/A	N/A
B748	5	114	41	0.66	N/A	N/A	N/A	N/A
B763	14	129	50	0.64	11	9.4	1.8	0.66
B772	7	91	26	0.71	N/A	N/A	N/A	N/A
B77W	15	96	34	0.65	9	2.7	1.3	0.49
B788	10	139	71	0.54	N/A	N/A	N/A	N/A
B789	12	125	64	0.54	N/A	N/A	N/A	N/A

N/A: Not available.